

# Multi-Sem Fusion: Multimodal Semantic Fusion for 3D Object Detection

Shaoqing Xu <sup>\* 1,2</sup>, Dingfu Zhou <sup>\* 2,3</sup>, Jin Fang <sup>2,3</sup>, Pengcheng Wang <sup>4</sup> and Liangjun Zhang <sup>2,3</sup>.

**Abstract**—LiDAR-based 3D Object detectors have achieved impressive performances in many benchmarks, however, multi-sensors (e.g., LiDAR and Camera) fusion-based techniques are promising to further improve the results. PointPainting, as a recently proposed framework, can add the semantic information from the 2D image into the 3D LiDAR point by the *painting* operation to boost the detection performance. However, due to the limited resolution of 2D feature maps, severe boundary-blurring effect (result from wrong semantic segmentation) happens during re-projection of 2D semantic segmentation into the 3D point clouds. To well handle this limitation, a general multimodal fusion framework *Multi-Sem Fusion (MSF)* has been proposed to fuse the semantic information from both the 2D image and 3D points scene parsing results. Specifically, MSF includes three main modules. First, state-of-the-art off-the-shelf 2D/3D semantic segmentation approaches are employed to generate the parsing results for 2D images and 3D point clouds. The 2D semantic information is further re-projected into the 3D point clouds with calibrated parameters. To handle the misalignment between the 2D and 3D parsing results, an Adaptive Attention-based Fusion (AAF) module is proposed to fuse them by learning an adaptive fusion score. Then the point cloud with the fused semantic label is sent to the following 3D object detectors. Furthermore, we propose a Deep Feature Fusion (DFF) module to aggregate deep features in different levels to boost the final detection performance. The effectiveness of the framework has been verified on two public large-scale 3D object detection benchmarks by comparing with different baselines. The experimental results show that the proposed fusion strategies can significantly improve the detection performance compared to the methods using only point clouds and the methods using only 2D semantic information. Most importantly, the proposed approach significantly outperforms other approaches and sets new state-of-the-art results on the nuScenes testing benchmark.

**Index Terms**—3D Object Detection, Multi-modal Fusion, Self-Attention

## I. INTRODUCTION

PERCEPTION of obstacles' 3D information via different types of sensors is a fundamental task in the field of computer vision and robotics. This topic has been extensively studied with the development of Autonomous Driving(AD) and intelligent transportation system. Though the LiDAR sensors have the superiority of providing distance information of the obstacles, the texture and color information has been totally lost due to the sparse scanning. Therefore, False Positive (FP)

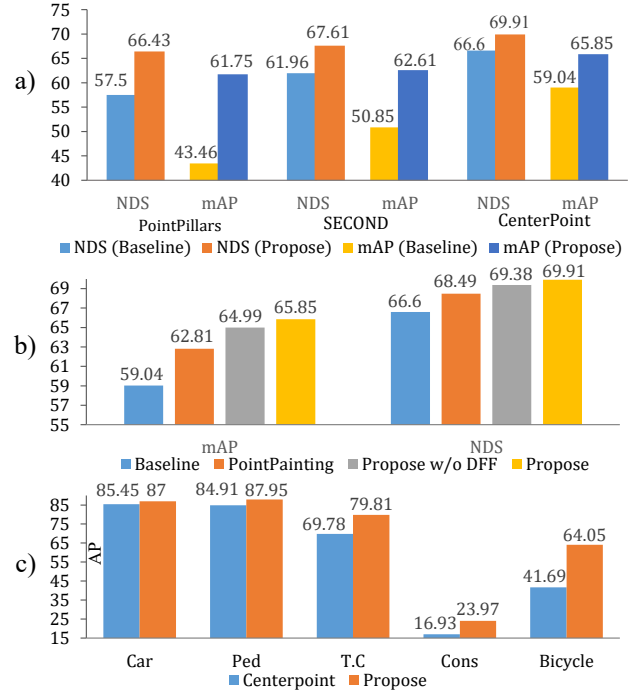


**Fig. 1:** The proposed *Multi-Sem Fusion (MSF)* is a general multimodal fusion framework which can be employed for different 3D object detectors. a) illustrate the improvements on three different baselines. b) gives the performance of *CenterPoint* [5] with the proposed modules on the public nuScenes benchmark. c) gives the improvements on different categories respectively. In addition, “w/o” represent “without” in short.

detection and wrong categories classification often happen for LiDAR-based object detection frameworks. In particular, with the development of the deep learning techniques on point-cloud-based representation, LIDAR-based approaches can be generally divided into point-based [1], voxel-based [2], [3], and hybrid-point-voxel-based methods [4].

On the contrary, the camera sensors can provide details texture and color information while the distance information has been totally lost during the perspective projection. The fusion of the two types of data is a promising way for boosting the perception performance of AD. Generally, multi-modal-based object detection approaches can be divided into early fusion-based [6], [7], deep fusion-based [8]–[10] and late fusion-based approaches [11]. Early fusion-based approaches aim at creating a new type of data by combining the raw data directly before sending them into the detection framework. Usually, these kinds of methods require pixel-level correspondence

<sup>1</sup> School of Transportation Science and Engineering, Beihang University, Beijing 100191, China.

<sup>2</sup> Robotics and Autonomous Driving Laboratory, Baidu Research.

<sup>3</sup> National Engineering Laboratory of Deep Learning Technology and Application, Beijing, China.

<sup>4</sup> School of Cyber Science and Technology, Beihang University, Beijing, 100191, China.

\* indicate equal contribution to this work.

between each type sensor data. Different from the early fusion-based methods, late fusion-based approaches fuse the detection results at the bounding box level. While deep fusion-based methods usually extract the features with different types of deep neural networks first and then fuse them at the features level. *PointPainting* [7] is an early fusion method which achieves superior detection results on different benchmarks. Specifically, The network takes point clouds together with the 2D image semantic predictions as inputs and output the detection results with any LiDAR-based 3D object detector. More importantly, it can be incorporated into any 3D object detectors regardless of point-based or voxel-based frameworks.

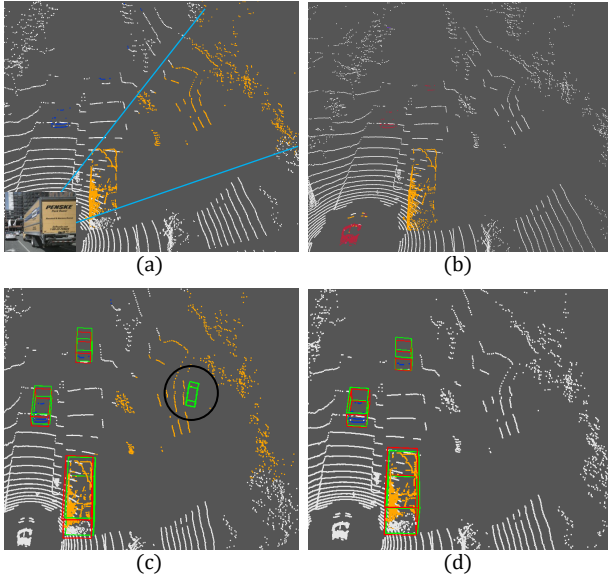


**Fig. 2:** (a) is the point cloud painted with the 2D segmentation results. The frustum within the blue line shows misclassified area due to the blurring effect at object’s boundary; (b) is the point cloud painted by 3D segmentation results (misclassified points are demonstrated in red color); (c) and (d) give the object detection results based on 2D painted point cloud (with an obvious False Positive (FP) Detection) and the proposed 2D/3D fusion framework respectively.

However, the blurring effect at object’s boundary often happens inevitably in image-based semantic segmentation methods. This effect becomes much worse when reprojecting the 2D semantic projections into the 3D point clouds. An example of this effect has been shown in Fig. 2. Taking the big truck at the left bottom of the sub-fig. 2-(a) as an example, we can find that there is a large frustum area of the background (e.g. points in orange color) that has been miss-classified as foreground due to the inaccurate projection results. In addition, the re-projection of 3D points to 2D image pixels is not exactly one-to-one because of the digital quantization and many-to-one projection issues. An interesting phenomenon is that the segmentation from the 3D point clouds (e.g., sub-fig. 2-(b)) performs much better at the boundary of obstacles. However, compared to the 2D image, the category classification from the 3D point cloud often gives worse results (e.g., point in red color) due to the detailed texture information has been lost in the point clouds.

The PointPainting, with 2D image semantic information,

has been proved to be effective for the 3D object detection task even with some semantic mistakes. An intuition idea is that whether the final detection performance can be further improved if both the 2D and 3D semantic results are fused together. Based on this idea, we propose a general multi-modal fusion framework *Multi-Seg Fusion* and try to fuse different types of sensors at the semantic level to improve the final 3D object detection performance. First of all, we obtain the 2D/3D semantic information throughout 2D/3D parsing approaches by taking images and raw point clouds. Each point in point cloud has two types of semantic information after projecting point clouds onto 2D semantic images based on the intrinsic and extrinsic calibration parameters., the semantic results conflict usually happens for a certain point, rather than concatenating the two types of information directly, an AAF strategy is proposed to fuse different kinds of semantic information in point or voxel-level adaptively based on the learned context features in a self-attention style. Specifically, an attention score has been learned for each point or voxel to balance the importance of the two different semantic results.

Furthermore, in order to detect obstacles with different sizes in an efficient way, a DFF module is proposed here to fuse the features at multi-scale receptive fields and a channel attention network to gather related channel information in the feature map. Then the fused features are passed for the following classification and regression heads to generate the final detection. As the results on nuScenes dataset are given in Fig. 1 (a), we can obviously find that the proposed modules can robustly boost the detection performance on different baselines. The results in Fig. 1(b) illustrates the contribution of each module we proposed and from this figure we can find that the detection results can be consistently improved by adding more modules gradually. Fig. 1 (c) shows the improvements on different categories and from this figure we can easily find that all the classes have been improved and “Bicycle” gets the most improvement (e.g., 22.3 points) on the nuScenes dataset.

This manuscript is an extension of the previously published conference paper [12] with a new review of the relevant state-of-the-art methods, new theoretical developments, and new experimental results. Compared to the previous conference paper, the 3D object detection accuracy has been improved with a large margin on the nuScenes 3D object detection benchmark by the submission of this manuscript. Furthermore, we also evaluate the proposed framework on the KITTT 3D object detection dataset and the experimental results on both public datasets prove the superiority of our framework. In general, the contributions of this work can be summarized as follows:

- 1) A general multi-modal fusion framework *Multi-Sem Fusion* has been proposed to fuse the different types of sensors in the semantic level to boost the 3D object detection performances.
- 2) Rather than combining different semantic results directly, an adaptive attention-based fusion module is proposed to fuse different kinds of semantic information in point or voxel-level by learning the fusion attention scores.
- 3) Furthermore, a deep features fusion module is also

proposed to fuse deep features at different levels for considering kinds of size object.

- 4) Finally, the proposed framework has been sufficiently verified on two public large-scale 3D object detection benchmarks and the experimental results show the superiority of the proposed fusion framework. The proposed method achieves SOTA results on the nuScenes dataset and outperforms other approaches with a big margin. Taking the proposed approach as the baseline, we have won the fourth nuScenes detection challenge held at ICRA 2021 on 3D Object Detection open track <sup>1</sup>.

## II. RELATED WORK

Generally, 3D object detection methods can be categorized as LiDAR-based, image-based [13] and multi-modal fusion-based, which takes LiDAR point cloud, image and multi-sensor captured data as inputs, respectively.

### A. LiDAR-based 3D Object Detection

The existing LiDAR-based 3D object detection methods can be generally categorized into three main groups as projection-based [14]–[18], voxel-based [2], [19]–[22] and point-based [3], [23], [24]. RangeRCNN [17] proposed a 3D range image-based 3D object detection framework where the anchors could be generated on the BEV (bird’s-eye-view) map. VoxelNet [2] is the first voxel-based framework, which uses a VFE (voxel feature encoding) layer to extract the point-level features for each voxel. To accelerate the inference speed, SECOND [19] presents a new framework which employs the sparse convolution [25] to replace the heavy 3D convolution operation. Inspired by the 2D anchor-free object detector CenterNet [26], CenterPoint [5] presented an anchor-free-based 3D object detector on LiDAR point cloud and achieved SOTA (state-of-the-art) performance on the nuScenes benchmark recently. To further improve the efficiency, PointPillars [3] divides the points into vertical columns (e.g., pillars) and extracts features from each pillar with the PointNet [27] module. Then, the feature map can be regarded as a pseudo image and all the 2D object detection pipelines can be applied for the 3D object detection task. Different from the regular representation like voxel or pseudo image, PointRCNN [1] directly extracts features from the raw points and generates the 3D proposals from the foreground points. Based on the PointRCNN, PV-RCNN [4] takes both the advantage from voxel and points representation and learns more discriminative features by employing both 3D voxel CNN and PointNet-based networks together.

### B. Camera-based 3D Object Detection

3D object detection can be achieved from stereo rigs [28] by detecting the 2D object from the image first and recovering the distance with traditional geometric stereo matching techniques [29]. Currently, with sufficient training data, the depth can be recovered from a single image [30]. Generally, the image-based 3D object detection methods with deep

learning techniques can be roughly divided into CAD Model-guided based, depth estimation-based and direct regression-based respectively. MANTA (Many-Tasks) [31] is proposed for many-task vehicle analysis from a given image, which can simultaneously output vehicle detection, part localization, visibility characterization and 3D dimension estimation etc. In [32], a large-scale dataset ApolloCar3D is provided for instance-level 3D car understanding. Based on this dataset, a key-points-based framework has been designed by extracting the key points first, and then the vehicle pose is obtained using a PnP solver. Furthermore, a novel work [13] leverages object proposals and shapes reconstruction with an end-to-end deep neural network. With the rapid development of depth estimation technology from a single image, leveraging the depth information for 3D object detection becomes popular. [33] and [34] compute the disparity map from stereo image pair and convert the depth maps to pseudo-LiDAR point clouds first and then any point cloud-based detectors can be employed for the 3D object detection task. The similar idea has been employed in [35], [36] and [37]. Instead of using CAD models or depth estimation, “SMOKE” [38] proposes to regress the 3D bounding box directly from the image and achieve promising performance on the KITTI benchmark. Based on this, [39] proposes a plug-and-play module IAFA to aggregate useful foreground information in an instance-aware manner for further improving the detection accuracy.

### C. Multi-sensors Fusion-based 3D Object Detection

The LiDAR can provide accurate distance information while the textures information has been lost. The camera sensor is just the opposite. In order to utilize the advantages of both sensors, many multi-sensor fusion-based approaches have been proposed. As mentioned in [40], the fusion approaches can be divided into model-based [41] and data-based approaches based on the way of fusing the sensor data. Generally, some model-based approaches have been used for tracking [42] while data-based approaches usually focus on modular environment perception tasks such as object detection [11], [43], [44]. For all fusion-based object detection approaches, also can be generally divided into three types: early fusion [43], late fusion [11] and deep fusion [44]. F-PointNet [24], PointFusion [9] and [43] are proposed to generate the object proposal in the 2D image first and then fuse the image features and point cloud for 3D BBox generation. PointPainting [7] is proposed to fuse the semantic information from the 2D image into the point cloud to boost the 3D point cloud object detectors. For achieving the parsing results, any SOTA approach can be used. AVOD [14], which is a typical late fusion framework, generates features that can be shared by RPN (region proposal network) and second stage refinement network. Multi-task fusion [45] [46] is also an effective technology, e.g., [23] jointing the semantic segmentation with 3D object detection tasks to further improve the performance. Furthermore, Radar and HDMaps are also employed for improving the detection accuracy. CenterFusion [47] focuses on the fusion of radar and camera sensors and associates the radar detections to objects on the image using a frustum-based association method and

<sup>1</sup><https://eval.ai/web/challenges/challenge-page/356/leaderboard/1012>



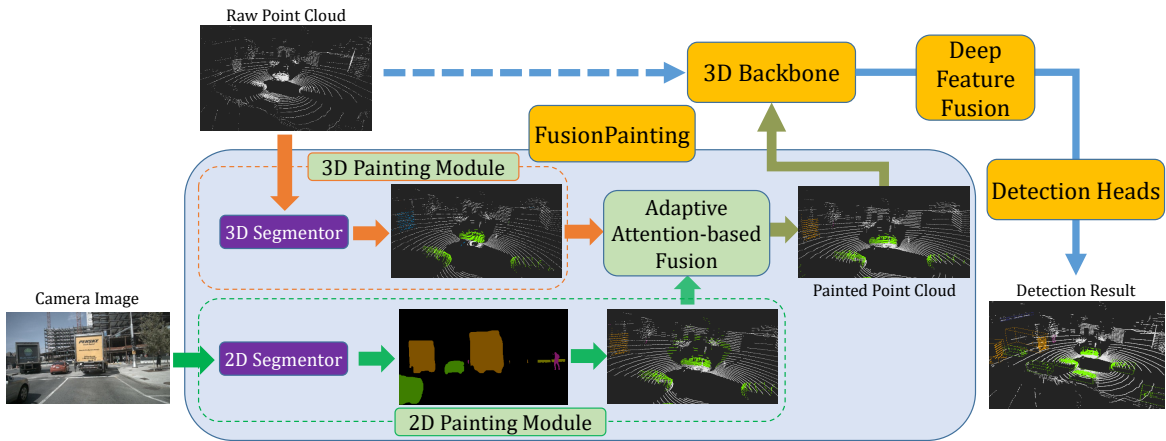


**Fig. 3:** Overview of the proposed *Multi-Sem Fusion* framework. We first process the input point clouds and 2D image with 2D and 3D parsing approaches to obtain the semantic information. Then, the proposed AAF module is adopted to fuse the two types of data at the semantic level. Furthermore, a DFF module is also proposed to fuse the deep features at different spatial levels to boost the detection for accurate kinds of size object. Finally, fused features are sent to the detection heads for producing the final detection results.

creates radar-based feature maps to complement the image features in a middle-fusion approach. In [48] and [49], the HDMaps are also taken as strong prior information for moving object detection in AD scenarios.

### III. MULTI-SEM FUSION FRAMEWORK

An overview of the proposed *Multi-Sem Fusion* framework is illustrated in Fig. 3. To fully explore the information from different sensors, we advocate fusing them at two different levels. First, the two types of information are early fused with the *PointPainting* technique by painting the point cloud with both the 2D and 3D semantic parsing results. To handle the inaccurate segmentation results, an AAF module is proposed to learn an attention score for different sensors for the following fusion purpose. By taking the points together with fused semantic information as inputs, deep features can be extracted from the backbone network. By considering that different size object requires different levels features, a novel DFF module is proposed to enhance the features with different levels for exploring the global context information and the local spatial details in a deep way. As shown in Fig. 3, the proposed framework consists of three main models as a multi-modal semantic segmentation module, an AAF module, and a DFF module. First of all, any off-the-shelf 2D and 3D scene parsing approaches can be employed to obtain the semantic segmentation from the RGB image and LiDAR point clouds respectively. Then the 2D and 3D semantic information are fused by the AAF module. Bypassing the points together with fused semantic labels into the backbone network, the DFF module is used to further improve the results by aggregating the features within different receptive fields and a channel attention module.

#### A. 2D/3D Semantic Parsing

*2D Image Parsing.* We can directly get rich texture and color information from 2D images, which can provide complementary information for the 3D point clouds. For acquiring 2D

semantic labels, a modern semantic segmentation network is employed for generating pixel-wise segmentation results. More importantly, the proposed framework is agnostic to specific segmentation model, and any state-of-the-art segmentation approaches can be employed here (e.g., [50]–[54], etc). We employ Deeplabv3+ [50] for generating the semantic results here. The network takes 2D images as input and outputs pixel-wise semantic classes scores for both the foreground instances and the background. Assuming that the obtained semantic map is  $S \in \mathbb{R}^{w \times h \times m}$ , where  $(w, h)$  is the image size and  $m$  is the number of category. By employing the intrinsic and extrinsic matrices, the 2D semantic information can be easily re-projected into the 3D point cloud. Specifically, by assuming the intrinsic matrix is  $\mathbf{K} \in \mathbb{R}^{3 \times 3}$ , the extrinsic matrix is  $\mathbf{M} \in \mathbb{R}^{3 \times 4}$  and the original 3D points clouds is  $\mathbf{P} \in \mathbb{R}^{N \times 3}$ , the projection of 3D point clouds from LiDAR to the camera can be obtained as Eq.(1) shown:

$$\mathbf{P}' = \text{Proj}(\mathbf{K}, \mathbf{M}, \mathbf{P}), \quad (1)$$

where  $\mathbf{P}'$  is the point in camera coordinate and “Proj” represents the projection process. By this projection, the parsing results from the 2D image can be assigned to its corresponding 3D points which is denoted by  $\mathbf{P}_{2D} \in \mathbb{R}^{N \times m}$ .

*3D Point Cloud Parsing.* As we have mentioned above, parsing results from the point clouds can well overcome the boundary blur influence while keeping the distance information. Similar to the 2D image segmentation, any SOTA 3D parsing approach can be employed here [55]–[57]. We employ the Cylinder3D [58] for generating the semantic results because of its impressive performance on the AD scenario. More importantly, the ground truth point-wise semantic annotations can be generated from the 3D object bounding boxes roughly as [1] while any extra semantic annotations are not necessary. Specifically, for foreground instances, the points inside a 3D bounding box are directly assigned with the corresponding class label while the points outside all the 3D bounding boxes are taken as the background. From this point of view, the proposed framework can work on any 3D detection benchmarks

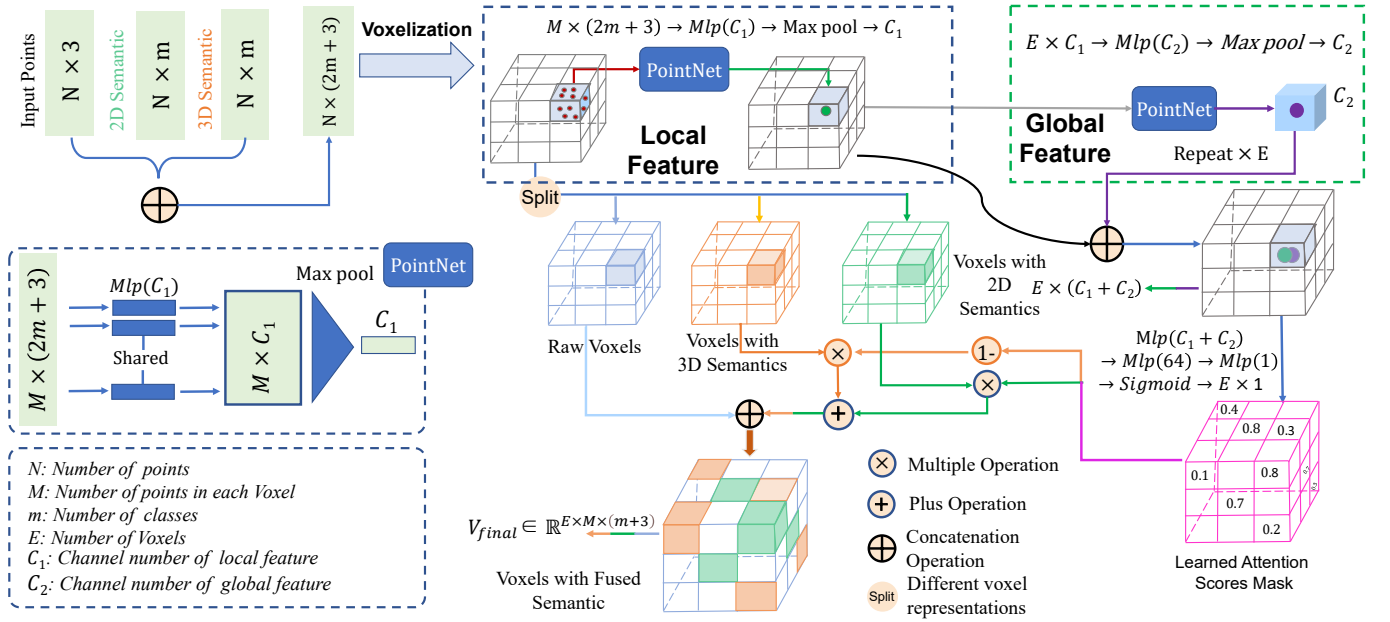


**Fig. 4:** The architecture of the proposed AAF module for 2D/3D semantic fusion. The input points and 2D/3D semantic results are first utilized to learn attention scores. Then, the raw points or voxel are painted with 2D/3D semantic labels adaptive by using the learned attention scores.

directly without any extra point-wise semantic annotations. After obtaining the trained network, we will obtain the parsing results which is denoted by  $\mathbf{P}_{3D} \in \mathbb{R}^{N \times m}$ .

### B. Adaptive Attention-based 2D/3D Semantic Fusion

As mentioned in previous work PointPainting, 2D semantic segmentation network have achieved impressive performance, however, the blurring effect at the shape boundary is also serious due to the limited resolution of the feature map (e.g.,  $\frac{1}{4}$  of the original image size). Therefore, the point clouds with 2D semantic segmentation usually has misclassified regions around the objects' boundary. For example, the frustum region is illustrated in the sub-fig. 2 (a) behind the big truck has been totally misclassified. On the contrary, the parsing results from the 3D point clouds usually can produce a clear and accurate object boundary e.g., sub-fig. 2(b). However, the disadvantages of the 3D segmentor are also obvious. One drawback is that without the color and texture information, the 3D segmentor is difficult to distinguish these categories with similar shapes from the point cloud-only. In order to boost advantages while suppressing disadvantages, an AAF module has been proposed to adaptively combine the 2D/3D semantic segmentation results. Then the fused semantic information is sent to the following 3D object detectors backbone to further extract the enhanced feature to improve the final detection results.

**AAF Module.** The detailed architecture of the proposed AAF module is illustrated in Fig. 4. By defining the input point clouds as  $\{\mathbf{P}_i, i = 1, 2, 3 \dots N\}$ , each point  $\mathbf{P}_i$  contains  $(x, y, z)$  coordinates and other optional information such as intensity. For simplicity, only the coordinates  $(x, y, z)$  are considered in the following context. Our goal is to find an efficient strategy to fuse semantic results from the 2D images and 3D

point clouds. Here, we propose to utilize the learned attention score to adaptively fuse the two types of results. Specifically, we first combine point clouds coordinate attributes  $(x, y, z)$  and 2D/3D labels with a concatenation operation to obtain a fused point clouds with the size of  $N \times (2m + 3)$ . For saving memory consumption, the following fusion is executed at the voxel level rather than the point level. Specifically, each point clouds has been divided into evenly distributed voxels and each voxel contains a fixed number of points. Here, we represent the voxels as  $\{V_i, i = 1, 2, 3 \dots E\}$ , where  $E$  is the total number of the voxels and each voxel  $V_i = (\mathbf{P}_i, \mathbf{V}_{2D}^i, \mathbf{V}_{3D}^i) \in \mathbb{R}^{M \times (2m+3)}$  containing a fixed number of  $M$  points with  $2m + 3$  features. Here,  $\mathbf{P}_i, \mathbf{V}_{2D}^i, \mathbf{V}_{3D}^i$  are point coordinates, predicted 2D and 3D semantic vectors in voxel level respectively. We employ the sampling technique to keep the same number of points in each voxel. Then, local and global feature aggregation strategies are applied to estimate an attention weight for each voxel for determining the importance of the 2D and 3D semantic labels.

In order to get local features, a PointNet [27]-like module is adopted to extract the voxel-wise information inside each non-empty voxel. For the  $i$ -th voxel, the local feature can be represented as:

$$V_i = f(p_1, p_2, \dots, p_M) = \max_{i=1, \dots, M} \{\text{MLP}_l(p_{i'})\} \in \mathbb{R}^{C_1}, \quad (2)$$

where  $\{p_{i'}, i' = 1, 2, 3 \dots M\}$  indicates the point inside each voxel.  $\text{MLP}_l(\cdot)$  and  $\max$  are the local multi-layer perceptron (MLP) networks and max-pooling operation. Specifically,  $\text{MLP}_l(\cdot)$  consists of a linear layer, a batch normalization layer, an activation layer and outputs local features with  $C_1$  channels. To achieve global feature information, we aggregate information based on the  $E$  voxels. In particular, we first use a  $\text{MLP}_g(\cdot)$  to map each voxel features from  $C_1$  dimension to

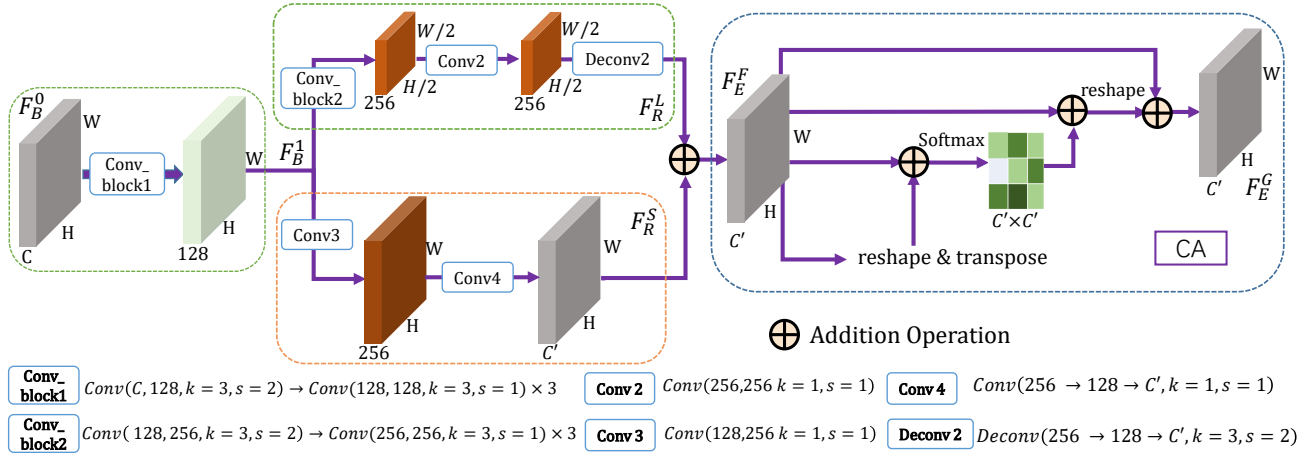


**Fig. 5:** An illustration of the proposed Deep Feature Fusion (DFF) module which includes one *fusion* module and one *channel attention* module respectively. The *fusion* module includes two branches for producing features with different field-of-view.

$C_2$  dimension. Then, another PointNet-like module is applied on all the voxels as:

$$V_{global} = f(V_1, V_2, \dots, V_E) = \max_{i=1, \dots, E} \{MLP_g(V_i)\} \in \mathbb{R}^{C_2}. \quad (3)$$

Finally, the global feature vector  $V_{global}$  is expanded to the same size of voxel number and then concatenate them to each local feature  $V_i$  to obtain final fused local and global features  $V_{gl} \in \mathbb{R}^{E \times (C_1 + C_2)}$ .

After getting fused features  $V_{gl}$  from the network, we need to estimate an attention score for each point in the voxel. This can be achieved by applying another MLP module  $MLP_{att}(\cdot)$  on  $V_{gl}$  and a Sigmoid activation function  $\sigma(\cdot)$ . Afterwards, we multiply the confidence score by corresponding one-hot semantic vectors for each voxel, which is denoted as Eq. (4), Eq. (5):

$$\mathbf{V}_{a.S}^i = \mathbf{V}_{2D}^i \times \sigma(MLP_{att}(V_{gl}^i)), \quad (4)$$

$$\mathbf{V}_{a.T}^i = \mathbf{V}_{3D}^i \times (1 - \sigma(MLP_{att}(V_{gl}^i))) \quad (5)$$

where  $\mathbf{V}_{2D}^i$  and  $\mathbf{V}_{3D}^i$  are the 2D and 3D semantic segmentation voxel labels which are encoded with one-hot format. The final semantic vector  $V_{final}^i$  of each voxel can be obtained by concatenating or element-wise addition of  $\mathbf{V}_{a.T}^i$  and  $\mathbf{V}_{a.S}^i$ .

### C. Deep Feature Fusion Module

In AD scenarios, we not only need to know what the object is but also where object it is, because both of them are very important for the following planning and control modules. In typical object detection frameworks, they correspond to the classification and regression branches respectively. Empirically, global context information is important to recognize the specific class attributes. On the contrary, the object's attributes (e.g., dimension, orientation, and precise location, etc) regression branch pays more attention to detailed spatial information around the ROI (region of interest) in a relatively small range. For accurate kinds of size object detection, therefore various scales receptive fields are necessary. This issue has been considered in most object detection frameworks. However,

how to use various field of view fields in an efficient way is vitally important.

To handle this kind of issue, a specific DFF module has been proposed to aggregate both the high-level and low-level features with different receptive fields. An illustration of the DFF module is shown in Fig. 5. First, the backbone features  $\mathbf{F}_B^0$  from the feature extractor pass the *Conv\_block1* with several convolution layers to obtain the  $\mathbf{F}_B^1$  as a basic feature. Here, *Conv\_block1* has four Conv modules and the first *conv* module takes  $C$  channels as input and outputs 128 channels, and the following three *conv*s share the same input channels and output channels. For each *conv* module in the Fig. 5, it consists one *Conv2d*, a batch normalization layer, and a Rectified Linear Unit (ReLU) activation layer. For easy understanding, we have given the stride and kernel size for each *conv* operation at the bottom of Fig. 5. Then, the feature  $\mathbf{F}_B^1$  will pass two branches to obtain the features with different receptive fields. For one branch, the features are down-sampled into 1/2 size with *Conv\_block2* first and then pass the *Conv2* operation. Finally, the outputs are up-sampled into the feature map  $\mathbf{F}_R^L \in \mathbb{R}^{H \times W \times C'}$  with *Deconv2*. For the other branch,  $\mathbf{F}_B^1$  will pass *Conv3* and *Conv4* to obtain the features of  $\mathbf{F}_R^S$  consecutively. And the shape of the output  $\mathbf{F}_R^L$  is the same as  $\mathbf{F}_R^S$ . Specially,  $C'$  can be  $C$ . After adding the high-level and low-level features element-wisely, a channel-attention (CA) module [59] is employed to further fuse both of them. The CA module selectively emphasizes interdependent channel maps by integrating relative features among all channel maps, so the  $\mathbf{F}_E^F$  can be fused better in a deep way. Finally,  $\mathbf{F}_E^G$  is taken as the inputs for the following classification and regression heads.

### D. 3D Object Detection Framework

The proposed AAF and DFF modules are detector independent and any off-the-shelf 3D object detectors can be directly employed as the baseline of our proposed framework. The 3D detector receives the points or voxels produced by the AAF module as inputs and can keep backbone structures unchanged to obtain the backbone features. Then, the backbone features

Methods	mAP (Mod.)(%)	Car $AP_{70}$ (%)			Pedestrian $AP_{70}$ (%)			Cyclist $AP_{70}$ (%)		
		Easy	Mod.	Hard	Easy	Mod.	Hard	Easy	Mod.	Hard
SECOND	66.64	90.04	81.22	78.22	56.34	52.40	46.52	83.94	66.31	62.37
SECOND *	68.11	91.04	82.31	79.31	59.28	54.18	50.20	85.11	67.52	63.36
Improvement	+1.47	+1.00	+1.09	+1.09	+2.94	+1.78	+3.68	+1.17	+1.54	+0.99
Pointpillars	62.90	87.59	78.17	75.23	53.58	47.58	44.04	82.21	62.95	58.66
PointPillars*	65.78	89.58	78.60	75.63	60.22	54.23	49.49	84.83	64.50	60.17
Improvement	+2.88	+1.99	+0.43	+0.4	+6.64	+6.65	+5.45	+2.62	+1.55	+1.51
PV-RCNN	71.82	92.23	83.10	82.42	65.68	59.29	53.99	91.57	73.06	69.80
PV-RCNN*	73.95	91.85	84.59	82.66	69.12	61.61	55.96	94.90	75.65	71.03
Improvement	+2.13	-0.38	+1.49	+0.24	+3.44	+2.32	+1.97	+3.33	+2.59	+1.23

**TABLE I:** 3D object detection evaluation on KITTI “val” split on different baseline approaches, where \* represents the boosted baseline by adding the proposed fusion modules. “Easy”, “Mod.” and “Hard” represent the three difficult levels defined by official benchmark and mAP (Mod.) represents the average AP of “Car”, “Pedestrian” and “Cyclist” on “Mod.” level. For easy understanding, we also highlight the improvements with different colors, where red represents an increase and green represents a decrease compared to the baseline method. This table is better to be viewed in color mode.

Methods	mAP (Mod.)(%)	Car $AP_{70}$ (%)			Pedestrian $AP_{70}$ (%)			Cyclist $AP_{70}$ (%)		
		Easy	Mod.	Hard	Easy	Mod.	Hard	Easy	Mod.	Hard
SECOND	71.95	92.31	88.99	86.59	60.5	56.21	51.25	87.30	70.65	66.63
SECOND *	73.72	94.70	91.62	88.35	63.95	59.66	55.81	91.95	73.28	67.75
Improvement	+2.90	+2.39	+2.63	+1.76	+3.45	+3.45	+4.56	+4.65	+2.63	+1.12
Pointpillars	69.18	92.50	87.80	87.55	58.58	52.88	48.30	86.77	66.87	62.46
PointPillars *	72.13	94.39	87.65	89.86	64.84	59.57	55.16	89.55	69.18	64.65
Improvement	+2.95	+1.89	-0.15	+2.31	+6.26	+6.69	+6.86	+2.78	+2.31	+2.19
PV-RCNN	76.23	94.50	90.62	88.53	68.67	62.49	58.01	92.76	75.59	71.06
PV-RCNN *	78.17	94.86	90.87	88.88	71.99	64.71	59.01	96.35	78.93	74.51
Improvement	+1.94	+0.36	+0.25	+0.35	+3.32	+2.22	+1.00	+3.59	+3.34	+3.45

**TABLE II:** Evaluation of bird’s-eye view object detection on KITTI “val” split with different baselines. Similar to the 3D detection, the red color represents an increase and the green color represents a decrease compared to the baseline method. This table is also better to be viewed in color mode.

are boosted by passing the proposed DFF module. Finally, detection results are generated from the classification and regression heads.

#### IV. EXPERIMENTAL RESULTS

To verify the effectiveness of our proposed framework, we evaluate it on two large-scale 3D object detection dataset in AD scenarios as KITTI [60] and nuScenes [61]. Furthermore, the proposed modules is also evaluated on different kinds of baselines for verifying its generalizability, including SECOND [19], PointPillars [3] and PVRCNN [4], etc.

##### A. Evaluation on KITTI Dataset

KITTI is one of the most popular benchmarks for 3D object detection in AD, which contains 7481 samples for training and 7518 samples for testing. The objects in each class are divided into three difficulty levels as “easy”, “moderate”, and “hard”, according to the object size, the occlusion ratio, and the truncation level. Since the ground truth annotations of the test samples are not available and the access to the test server is limited, we follow the idea in [44] and split the training data into “train” and “val” where each set contains 3712 and 3769 samples respectively. In this dataset, both the LiDAR point clouds and the RGB images have been provided. In addition, both the intrinsic parameters and extrinsic parameters between different sensors have been given.

**Evaluation Metrics.** We follow the official metrics provided by the KITTI for evaluation.  $AP_{70}$  is used for “Car” category while  $AP_{50}$  is used for “Pedestrian” and “Cyclist”. Specifically, before the publication of [62], the KITTI official benchmark used the 11 recall positions for comparison. After that, the official benchmark changes the evaluation criterion from 11-points to 40-points because the latter one is proved to be more stable than the former [62]. Therefore, we use the 40-points criterion for all the experiments here. In addition, similar to [7], the average AP (mAP) of three Classes for “Moderate” is also taken as an indicator for evaluating the average performance on all three classes.

**Baselines.** Three different baselines have been used for evaluation on KITTI:

- 1) *SECOND* [19] is the first to employ the sparse convolution on the voxel-based 3D object detection framework to accelerate the efficiency of LiDAR-based 3D object detection.
- 2) *PointPillars* [3] is proposed to further improve the detection efficiency by dividing the point cloud into vertical pillars rather than voxels. For each pillar, *Pillar Feature Net* is applied to extract the point-level feature.
- 3) *PV-RCNN* [4] is a hybrid point-voxel-based 3D object detector, which can utilize the advantages from both the point and voxel representations.

**Implementation Details.** DeeplabV3+ [63] and Cylinder3D [64] are employed for 2D and 3D scene parsing respectively.



Methods	NDS (%)	mAP (%)	AP (%)									
			Car	Pedestrian	Bus	Barrier	T.C.	Truck	Trailer	Moto.	Cons.	Bicycle
SECOND [19]	61.96	50.85	81.61	77.37	68.53	57.75	56.86	51.93	38.19	40.14	17.95	18.16
SECOND*	67.61	62.61	84.77	83.36	72.41	63.67	74.99	60.32	42.89	66.50	23.59	54.62
Improvement $\uparrow$	<b>+5.65</b>	<b>+11.76</b>	<b>+3.16</b>	<b>+5.99</b>	<b>+3.88</b>	<b>+5.92</b>	<b>+18.13</b>	<b>+8.39</b>	<b>+4.70</b>	<b>+26.36</b>	<b>+5.64</b>	<b>+36.46</b>
PointPillars [3]	57.50	43.46	80.67	70.80	62.01	49.23	44.00	49.35	34.86	26.74	11.64	5.27
PointPillars*	66.43	61.75	84.79	83.41	70.52	59.42	75.43	57.50	42.32	66.97	22.43	54.68
Improvement $\uparrow$	<b>+8.93</b>	<b>+18.29</b>	<b>+4.12</b>	<b>+12.61</b>	<b>+8.51</b>	<b>+10.19</b>	<b>+31.43</b>	<b>+8.15</b>	<b>+7.46</b>	<b>+40.23</b>	<b>+10.79</b>	<b>+49.41</b>
CenterPoint [5]	64.82	56.53	84.73	83.42	66.95	64.56	64.76	54.52	36.13	56.81	15.81	37.57
CenterPoint*	69.91	65.85	87.00	87.95	71.53	67.14	79.89	61.91	41.22	73.85	23.97	64.06
Improvement $\uparrow$	<b>+5.09</b>	<b>+6.81</b>	<b>+2.77</b>	<b>+4.53</b>	<b>+4.58</b>	<b>+2.58</b>	<b>+15.13</b>	<b>+7.39</b>	<b>+5.09</b>	<b>+17.04</b>	<b>+8.16</b>	<b>+26.49</b>

**TABLE III:** Evaluation results on nuScenes validation dataset. “NDS” and “mAP” mean nuScenes detection score and mean Average Precision. “T.C.”, “Moto.” and “Cons.” are short for “traffic cone”, “motorcycle”, and “construction vehicle” respectively. “\*” denotes the improved baseline by adding the proposed fusion module. The red color represents an increase compared to the baseline. This table is also better to be viewed in color mode.

More details, the DeeplabV3+ is pre-trained on Cityscape<sup>2</sup>, and the Cylinder3D is trained on KITTI point clouds by taking points in 3D ground trues bounding box as foreground annotation. For AAF module,  $m = 4$ ,  $C_1 = 64$ ,  $C_2 = 128$ , respectively. The voxel size for PointPillars and SECOND are  $0.16m \times 0.16m \times 4m$  and  $0.05m \times 0.05m \times 0.1m$  respectively. In addition, both of the two baselines use the same optimization (e.g., AdamW) and learning strategies (e.g., one cycle) for all the experiments. In the DFF module, we set  $C = 256$  and  $C' = 512$  for *SECOND* and *PV-RCNN* framework and  $C = 64$  and  $C' = 384$  for *PointPillars* network. The kernel and stride size are represented with  $k$  and  $s$  in Fig.5, respectively.

The proposed approach is implemented with PaddlePaddle [65] and all the methods are trained on NVIDIA Tesla V100 with 8 GPUs. The AdamW is taken as the optimizer and the one-cycle learning strategy is adopted for training the network. For *SECOND* and *PointPillars*, the batch size is 4 per GPU and the maximum learning rate is 0.003 while the bath size is 2 per GPU and the maximum learning rate is 0.001 for *PV-RCNN*.

**Quantitative Evaluation.** We illustrate the results on 3D detection and Bird’s-eye view in Tab. I and Tab. II respectively. From the table, we can clearly see that remarkable improvements have been achieved on the three baselines across all the categories. Taking Pointpillars as an example, the proposed method has achieved 0.43%, 6.65%, 1.55% points improvements on “Car”, “Pedestrian” and “Cyclist” respectively. Interestingly, compared to “Car”, “Pedestrian” and “Cyclist” give much more improvements by the fusion painting modules.

### B. Evaluation on the nuScenes Dataset

The nuScenes [61] is a recently released large-scale (with a total of 1,000 scenes) AD benchmark with different kinds of information including LiDAR point cloud, radar point, Camera images, and High Definition Maps, etc. For a fair comparison, the dataset has been divided into “train”, “val”, and “test” three subsets officially, which includes 700 scenes (28130 samples), 150 scenes (6019 samples), and 150 scenes (6008 samples)

respectively. Objects are annotated in the LiDAR coordinate and projected into different sensors’ coordinates with pre-calibrated intrinsic and extrinsic parameters. For the point clouds stream, only the keyframes (2fps) are annotated. With a 32 lines LiDAR scanner, each frame contains about 300,000 points for 360-degree viewpoint. For the object detection task, the obstacles have been categorized into 10 classes as “car”, “truck”, “bicycle” and “pedestrian” etc. Besides the point clouds, the corresponding RGB images are also provided for each keyframe, and for each keyframe, there are 6 cameras that can cover 360 fields of view.

**Evaluation Metrics.** The evaluation metric for nuScenes is totally different from KITTI and they propose to use mean Average Precision (mAP) and nuScenes detection score (NDS) as the main metrics. Different from the original mAP defined in [71], nuScenes consider the BEV center distance with thresholds of {0.5, 1, 2, 4} meters, instead of the IoUs of bounding boxes. NDS is a weighted sum of mAP and other metric scores, such as average translation error (ATE) and average scale error (ASE). For more details about the evaluation metric please refer to [61].

**Baselines.** We have integrated the proposed module on three different SOTA baselines to verify its effectiveness. Similar to the KITTI dataset, both the *SECOND* and *PointPillars* are employed and the other detector is *CenterPoint* [5], which is the first anchor-free-based 3D object detector for LiDAR-based 3D object detection.

**Implementation Details** HTCNet [52] and Cylinder3D [64] are employed here for obtaining the 2D and 3D semantic segmentation results respectively. We used the HTCNet model trained on nuImages<sup>3</sup> dataset directly for generating the semantic labels. For Cylinder3D, we train it directly on the nuScenes 3D object detection dataset while the point cloud semantic label is produced by taking the points inside each bounding box. In AAF module,  $m = 11$ ,  $C_1 = 64$  and  $C_2 = 128$  respectively. In DFF module,  $C = 256$  and  $C' = 512$  for *SECOND* and *CenterPoint* while  $C = 64$  and  $C' = 384$  for *PointPillars*. The setting for kernel size  $k$  and stride  $s$  are given in Fig. 5 and same for all three detectors. The voxel size for PointPillars, SECOND and CenterPoint are  $0.2m \times 0.2m \times 8m$ ,  $0.1m \times 0.1m \times 0.2m$  and

<sup>2</sup><https://www.cityscapes-dataset.com>

<sup>3</sup><https://www.nuscenes.org/nuimages>



Methods	Modality	NDS(%)	mAP(%)	AP (%)									
				Car	Truck	Bus	Trailer	Cons	Ped	Moto	Bicycle	T.C	Barrier
PointPillars [7]	L	55.0	40.1	76.0	31.0	32.1	36.6	11.3	64.0	34.2	14.0	45.6	56.4
3DSSD [66]	L	56.4	46.2	81.2	47.2	61.4	30.5	12.6	70.2	36.0	8.6	31.1	47.9
CBGS [67]	L	63.3	52.8	81.1	48.5	54.9	42.9	10.5	80.1	51.5	22.3	70.9	65.7
HotSpotNet [68]	L	66.0	59.3	83.1	50.9	56.4	53.3	23.0	81.3	63.5	36.6	73.0	71.6
CVCNET [69]	L	66.6	58.2	82.6	49.5	59.4	51.1	16.2	83.0	61.8	38.8	69.7	69.7
CenterPoint [5]	L	67.3	60.3	85.2	53.5	63.6	56.0	20.0	54.6	59.5	30.7	78.4	71.1
PointPainting [7]	L & C	58.1	46.4	77.9	35.8	36.2	37.3	15.8	73.3	41.5	24.1	62.4	60.2
3DCVF [70]	L & C	62.3	52.7	83.0	45.0	48.8	49.6	15.9	74.2	51.2	30.4	62.9	65.9
Our proposed	L & C	<b>71.6</b>	<b>68.2</b>	<b>87.1</b>	<b>60.8</b>	<b>66.5</b>	<b>61.7</b>	<b>30.0</b>	<b>88.3</b>	<b>74.7</b>	<b>53.5</b>	<b>85.0</b>	<b>71.8</b>

**TABLE IV:** Comparison with other SOTA methods on the nuScenes 3D object detection testing benchmark. “L” and “C” in the modality column represent LiDAR and Camera sensors respectively. For easy understanding, the highest score in each column is shown in bold font. To be clear, only the results with publications are listed here.

$0.075m \times 0.075m \times 0.075m$ , respectively. We use AdamW [72] as the optimizer with the max learning rate is 0.001. Following [61], 10 previous LiDAR sweeps are stacked into the keyframe to make the point clouds more dense.

All the baselines are trained on NVIDIA Tesla V100 (8 GPUs) with a batch size of 4 per GPU for 20 epochs. AdamW is taken as the optimizer and the one-cycle learning strategy is adopted for training the network with the maximum learning rate is 0.001.

**Quantitative Evaluation.** The proposed framework has been evaluated on nuScenes benchmark for both “val” and “test” splits. The results of comparison with three baselines are given in Tab. III. From this table, we can see that significant improvements have been achieved on both the mAP and NDS across all the three baselines. For the *PointPillars*, the proposed module gives **8.93** and **18.29** points improvements on NDS and mAP respectively. For *SECOND*, the two values are **5.65** and **11.76** respectively. Even for the strong baseline *CenterPoint*, the proposed module can also give **5.09** and **9.32** points improvements. In addition, we also find that the categories which share small sizes such as “Traffic Cone”, “Moto” and “Bicycle” have received more improvements compared to other categories. Taking “Bicycle” as an example, the mAP has been improved by 36.46%, 49.41% and 26.49% compared to *SECOND*, *PointPillar* and *Centerpoint* respectively. This phenomenon can be explained as these categories with small sizes are hard to be recognized in point clouds because of a few LiDAR points on them. In this case, the semantic information from the 2D/3D parsing results is extremely helpful for improving 3D object detection performance. It should be emphasized that the result in Tab. III without any Test Time Augmentation(TTA) strategies.

To compare the proposed framework with other SOTA methods, we submit our results (adding fusion modules on *CenterPoint*) on the nuScenes evaluation sever<sup>4</sup> for test split. The detailed results are given in Tab. IV. From this table, we can find that the proposed method achieves the best performance on both the mAP and NDS scores. Compared to the baseline *CenterPoint*, 4.3 and 7.9 points improvements have been achieved by adding our proposed fusion modules. For easy understanding, we have highlighted the best performances

in bold in each column. It should be noted that the results in Tab. IV the Test Time Augmentation(TTA) strategy including multiple flip and rotation operations is applied during the inference time which is 1.69 points higher than the origin method of ours.

### C. Ablation Studies

To verify the effectiveness of different modules, a series of ablation experiments have been designed to analyze the contribution of each component for the final detection results. Specially, three types of experiments are given as *different semantic representations* and *different fusion modules* and *effectiveness of channel attention*.

Representations	mAP (%)	NDS (%)
PointPillar [3]	43.46	57.50
Semantic ID	50.96 (+7.50)	60.69 (+3.19)
Onehot Vector	52.18 (+8.72)	61.59 (+4.09)
Semantic Score	53.10 (+9.64)	62.20 (+4.70)

**TABLE V:** Ablation studies on the nuScenes [60] dataset for fusing the semantic results with different representations.

**Different Semantic Representations.** First of all, we investigate the influence of the different semantic result representations on the final detection performance. Three different representations as “Semantic ID”, “Onehot Vector” and “Semantic Score” are considered here. For “Semantic ID”, the digital class ID is used directly and for the “Semantic Score”, the predicted probability after the Softmax operation is used. In addition, to convert the semantic scores to a “Onehot Vector”, we assign the class with the highest score as “1” and keep other classes as “0”. Here, we just add the semantic feature to the original  $(x, y, z)$  coordinates with concatenation operation and *PointPillars* is taken as the baseline on nuScenes dataset due to its efficiency of model iteration. From the results in Tab. V, we can easily find that the 3D semantic information can significantly boost the final object detection performance regardless of different representations. More specifically, the “Semantic Score” achieves the best performance among the three which gives 9.64 and 4.70 points improvements for **mAP** and **NDS** respectively. We guess that the semantic score can provide more information than the other two representations because it not only provides the class ID but also the confidence for all the classes.

<sup>4</sup><https://www.nuscenes.org/object-detection/>

**Different Fusion Modules.** We also execute different experiments to analyze the performances of each fusion module on both KITTI and nuScene dataset. The *SECOND* is chosen as the baseline for KITTI while all the three detectors are verified on nuScene. The results are given in Tab. VI and Tab. VII for KITTI and nuScenes respectively. To be clear, the “3D Sem” and “2D Sem.” represent the 2D and 3D parsing results. “AAF” represents the fusion of the 2D and 3D semantic information with the proposed adaptive attention module and the “AAF + DFF” represents the module with both the two fusion strategies.

Strategies	AP(%)			mAP(%)
	Car.(Mod.)	Ped.(Mod.)	Cyc.(Mod.)	
SECOND [19]	88.99	56.21	70.65	71.95
3D Sem.	+ 0.81	+ 0.70	+ 0.63	+ 0.71
2D Sem.	+ 1.09	+ 1.35	+ 1.20	+ 1.41
AAF	+ 1.62	+ 1.78	+ 1.91	+ 1.77
AAF & DFF	+ 2.63	+ 3.45	+ 2.63	+ 2.90

**TABLE VI:** Evaluation of ablation studies on the public KITTI [60] dataset. Similar to PointPainting [7], we provide the 2D BEV detection here. To be clear, only the results of “Mod” have been given and **mAP** is the average mean of all the three categories.

Strategies	SECOND		PointPillars		CenterPoint	
	mAP(%)	NDS(%)	mAP(%)	NDS(%)	mAP(%)	NDS(%)
SECOND	50.85	61.96	43.46	57.50	56.53	64.82
3D Sem.	+ 3.60	+ 1.45	+ 8.72	+ 4.09	+ 4.59	+ 1.86
2D Sem.	+ 8.55	+ 4.07	+15.64	+ 7.55	+ 6.28	+ 3.67
AAF	+ 11.30	+ 5.45	+17.31	+ 8.54	+ 8.46	+ 4.56
AAF & DFF	+ 11.76	+ 5.65	+ 18.19	+ 8.93	+ 9.32	+ 5.09

**TABLE VII:** Ablation studies for different fusion strategies on the nuScenes benchmark. The first row is the performance of the baseline method and the following values are the gains obtained by adding different modules.

In Tab. VI, the first row is the performance of the baseline method and the following values are the gains obtained by adding different modules. From the table, we can obviously find that all the modules give positive effects on all three categories for the final detection results. For all the categories, the proposed modules give 2.9 points improvements averagely and “Pedestrian” achieves the most gain which achieves 3.45 points. Furthermore, we find that deep fusion gives the most improvements compared to the other three modules in this dataset.

Tab. VII gives the results on the nuScenes dataset. To be clear, a boosted version of baseline is presented here than in [12] by fixing the sync-bn issue in the source code. From this table, we can see that both the 2D and 3D semantic information can significantly boost the performances while the 2D information provide more improvements than the 3D information. This phenomenon can be explained as that the 2D texture information can highly benefit the categories classification results which is very important for the final **mAP** computation. In addition, by giving the 2D information, the recall ability can be improved especially for objects in long distance with a few scanned points. In other words, the advantage for 3D semantic information is that the point clouds can well handle the occlusion among objects which

are very common in AD scenarios which is hard to deal with in 2D. After fusion, all the detectors achieve much better performances than only one semantic information (2D or 3D).

Furthermore, a deep fusion module is also proposed to aggregate the backbone features to further improve the performance. From the Tab. Tab. VI and Tab. VII, we find that the deep fusion module can slightly improve the results for all three baseline detectors. Interestingly, compared to the *SECOND* and *PointPillars*, *CenterPoint* gives much better performance by adding the deep fusion module. This can be explained that the large deep backbone network in *CenterPoint* gives much deeper features that are more suitable for the proposed deep feature fusion module.

Strategies	AP(%)			mAP(%)
	Car.(Mod.)	Ped.(Mod.)	Cyc.(Mod.)	
SECOND	88.99	56.21	70.65	71.95
One scale CA	89.68 (+0.69)	57.77 (+1.56)	71.39 (+0.74)	73.70 (+1.75)
Multi-scale CA	90.22 (+1.23)	58.11 (+1.90)	71.77 (+1.12)	74.41 (+2.46)

**TABLE VIII:** Ablation with/without multi-scale channel attention (CA) on KITTI dataset. The meaning of *one-scale CA* is we just use  $F_R^L$  to the CA module. And multi-scale denote that we use both fused  $F_R^L$  and  $F_R^S$  feature to the next module.

**Effectiveness of Multi-scale CA.** In addition, a small experiment is also designed for testing the effectiveness of multi-scale attention in the DFF module. *SECOND* is taken as the baseline and tested on the KITTI dataset. From the results given in Tab. VIII, we can see that by employing the one-scale features, the **mAP** has been improved by 1.75 points compared to the baseline. By adding the multi-scale operation, additional 0.71 points improvements can be further obtained.

*D. Computation Time*

Types	PointPillars	SECOND
Baseline	53.5 (ms)	108.2 (ms)
+3D Sem	+3.0 (ms)	+0.5 (ms)
+2D Sem	+3.4 (ms)	+0.2 (ms)
The Proposed	62.5 (ms)	113.3 (ms)

**TABLE IX:** Inference time of different modules. Here, +3D Sem and +2D Sem denote the time of adding 3D/2D semantic information to input data. *The Proposed* denotes the proposed framework with the modules including two types of semantic information and AAF & DFF modules.

Besides the performance, the computation time is also very important. Here, we test the computation time of each module based on the *PointPillars* and *SECOND* on the KITTI dataset in Tab. IX. For a single Nvidia V100 GPU, the *PointPillars* takes 53.5 ms per frame. By adding the 2D and 3D semantic information, the inference time increases 3.0 ms and 3.4 ms respectively while the time increases about 9 ms by adding two types semantic information and the AAF & DFF modules. The inference time for *SECOND* is given at the right column of Tab. IX. Compared with the baseline, the 2D/3D semantic segmentation information gives nearly no extra computational burden. We explain this phenomenon as that in *SECOND* the simple *mean* operation is employed for extracting the features for each voxel and the computation time of this operation

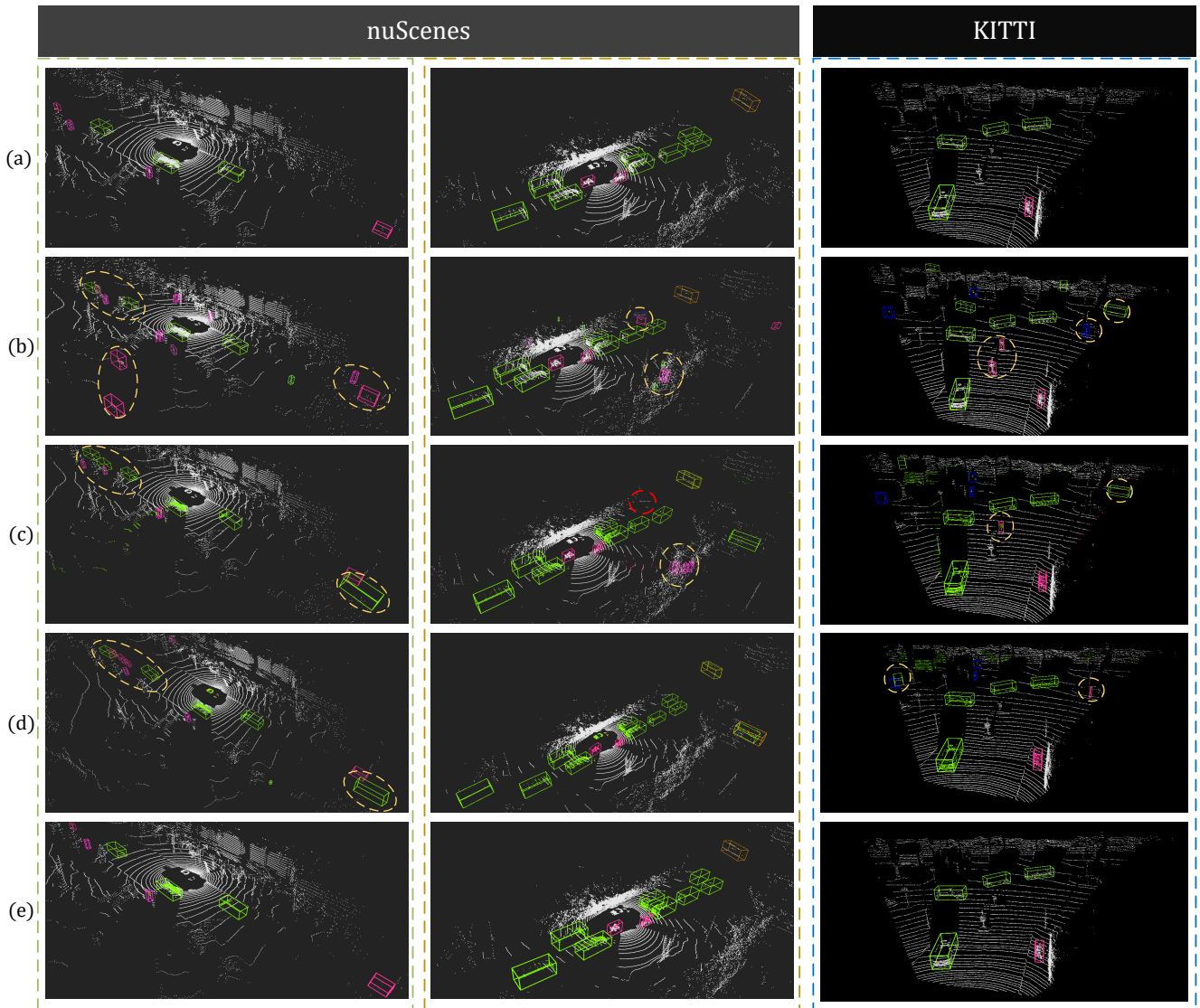


**Fig. 6:** Visualization of detection results with Open3d [73], where (a) is the ground-truth, (b) is the baseline method based on only point cloud, (c), (d) and (e) are the detection results based on the 2D semantic, 3D semantic and fusion semantic information, respectively. Especially, the yellow and red dash ellipses show some false positive and false negative detection. For nuScenes dataset, the baseline detector used here is CenterPoint, and for KITTI is SECOND.

will not change too much with the increasing of the feature dimension. For *PointPillars*, the MPL is employed for feature extracting in each pillar, therefore the computation time will increase largely with the increasing of the feature dimension.

In addition, we also record the time used for obtaining the 2D/3D semantic results. For Deeplab V3+, the inference time is about 32 ms per frame while for Cylinder3D, it takes about 140 ms per frame. Furthermore, the re-projection of 2D image to 3D point clouds also takes about 3 ms for each frame. The almost time consuming here are 2D/3D point clouds segmentation operations. But in the practical using there just need a extra segmentation head after detection network backbone. In other words, multi-head is needed here for both detection and segmentation task. These just taking few milliseconds when using model inference acceleration operation, like C++ inference library TensorRT.

### E. Qualitative Detection Results

We show some qualitative detection results on nuScenes and KITTI dataset in Fig. 6 in which Fig. 6 (a) is the ground truth, (b), (c), and (d) are the detect result of baseline (CenterPoint) without any extra information, with 2D and 3D semantic information respectively and (e) is final results with all the fusion modules. From these figures, we can easily find that there is some false positive detection caused by the frustum blurring effect in 2D painting, while the 3D semantic results give a relatively clear boundary of the object but provides some worse class classification. More importantly, the proposed framework which combines both the two complementary information from 2D and 3D segmentation can give much more accurate detection results.



## V. CONCLUSION AND FUTURE WORKS

In this work, we proposed an effective framework *Multi-Sem Fusion* to fuse the RGB image and LiDAR point clouds in two different levels. For the first level, the proposed AAF module aggregates the semantic information from both the 2D image and 3D point clouds segmentation results adaptively with learned weight scores. For the second level, a DFF module is proposed to further fuse the boosted feature maps with different receptive fields by a channel attention module. Thus, the features can cover objects of different sizes. More importantly, the proposed modules are detector independent which can be seamlessly employed in different frameworks. The effectiveness of the proposed framework has been evaluated on public benchmark and outperforms the state-of-the-art approaches. However, the limitation of the current framework is also obvious that both the 2D and 3D parsing results are obtained by offline approaches which prevent the application of our approach in real-time AD scenarios. An interesting research direction is to share the backbone features for both object detection and segmentation and take the segmentation as an auxiliary task.

## REFERENCES

- [1] S. Shi, X. Wang, and H. Li, "Pointcnn: 3d object proposal generation and detection from point cloud," in *IEEE/CVF Conference on Computer Vision and Pattern Recognition*, pp. 770–779, 2019. [1](#), [3](#), [4](#)
- [2] Y. Zhou and O. Tuzel, "Voxelnet: End-to-end learning for point cloud based 3d object detection," in *IEEE Conference on Computer Vision and Pattern Recognition*, pp. 4490–4499, 2018. [1](#), [3](#)
- [3] A. H. Lang, S. Vora, H. Caesar, L. Zhou, J. Yang, and O. Beijbom, "Pointpillars: Fast encoders for object detection from point clouds," in *IEEE Conference on Computer Vision and Pattern Recognition*, pp. 12697–12705, 2019. [1](#), [3](#), [7](#), [8](#), [9](#)
- [4] S. Shi, C. Guo, L. Jiang, Z. Wang, J. Shi, X. Wang, and H. Li, "Pv-rcnn: Point-voxel feature set abstraction for 3d object detection," in *IEEE Conference on Computer Vision and Pattern Recognition*, pp. 10529–10538, 2020. [1](#), [3](#), [7](#)
- [5] T. Yin, X. Zhou, and P. Krahenbühl, "Center-based 3d object detection and tracking," *IEEE Conference on Computer Vision and Pattern Recognition*, 2021. [1](#), [3](#), [8](#), [9](#)
- [6] J. Dou, J. Xue, and J. Fang, "Seg-voxelnet for 3d vehicle detection from rgb and lidar data," in *2019 International Conference on Robotics and Automation (ICRA)*, pp. 4362–4368, IEEE, 2019. [1](#)
- [7] S. Vora, A. H. Lang, B. Helou, and O. Beijbom, "Pointpainting: Sequential fusion for 3d object detection," in *IEEE/CVF Conference on Computer Vision and Pattern Recognition*, pp. 4604–4612, 2020. [1](#), [2](#), [3](#), [7](#), [9](#), [10](#)
- [8] Z. Zhang, M. Zhang, Z. Liang, X. Zhao, M. Yang, W. Tan, and S. Pu, "Maff-net: Filter false positive for 3d vehicle detection with multi-modal adaptive feature fusion," *arXiv preprint arXiv:2009.10945*, 2020. [1](#)
- [9] D. Xu, D. Anguelov, and A. Jain, "Pointfusion: Deep sensor fusion for 3d bounding box estimation," in *IEEE Conference on Computer Vision and Pattern Recognition*, pp. 244–253, 2018. [1](#), [3](#)
- [10] Y. Tian, K. Wang, Y. Wang, Y. Tian, Z. Wang, and F.-Y. Wang, "Adaptive and azimuth-aware fusion network of multimodal local features for 3d object detection," *Neurocomputing*, vol. 411, pp. 32–44, 2020. [1](#)
- [11] S. Pang, D. Morris, and H. Radha, "Clocs: Camera-lidar object candidates fusion for 3d object detection," in *2020 IEEE/RSJ International Conference on Intelligent Robots and Systems (IROS)*, IEEE, 2020. [1](#), [3](#)
- [12] S. Xu, D. Zhou, J. Fang, J. Yin, Z. Bin, and L. Zhang, "Fusionpainting: Multimodal fusion with adaptive attention for 3d object detection," in *IEEE Intelligent Transportation Systems Conference*, 2021. [2](#), [10](#)
- [13] J. Ku, A. D. Pon, and S. L. Waslander, "Monocular 3d object detection leveraging accurate proposals and shape reconstruction," in *IEEE Conference on Computer Vision and Pattern Recognition*, pp. 11867–11876, 2019. [3](#)
- [14] J. Ku, M. Mozifian, J. Lee, A. Harakeh, and S. L. Waslander, "Joint 3d proposal generation and object detection from view aggregation," in *2018 IEEE/RSJ International Conference on Intelligent Robots and Systems*, pp. 1–8, IEEE, 2018. [3](#)
- [15] W. Luo, B. Yang, and R. Urtasun, "Fast and furious: Real time end-to-end 3d detection, tracking and motion forecasting with a single convolutional net," in *IEEE conference on Computer Vision and Pattern Recognition*, pp. 3569–3577, 2018. [3](#)
- [16] B. Yang, W. Luo, and R. Urtasun, "Pixor: Real-time 3d object detection from point clouds," in *IEEE conference on Computer Vision and Pattern Recognition*, pp. 7652–7660, 2018. [3](#)
- [17] Z. Liang, Z. Zhang, M. Zhang, X. Zhao, and S. Pu, "RangeiouDET: Range image based real-time 3d object detector optimized by intersection over union," in *Proceedings of the IEEE/CVF Conference on Computer Vision and Pattern Recognition*, pp. 7140–7149, 2021. [3](#)
- [18] P. Hu, J. Ziglar, D. Held, and D. Ramanan, "What you see is what you get: Exploiting visibility for 3d object detection," in *IEEE Conference on Computer Vision and Pattern Recognition*, pp. 11001–11009, 2020. [3](#)
- [19] Y. Yan, Y. Mao, and B. Li, "Second: Sparsely embedded convolutional detection," *Sensors*, vol. 18, no. 10, p. 3337, 2018. [3](#), [7](#), [8](#), [10](#)
- [20] H. Kuang, B. Wang, J. An, M. Zhang, and Z. Zhang, "Voxel-fpn: Multi-scale voxel feature aggregation for 3d object detection from lidar point clouds," *Sensors*, vol. 20, no. 3, p. 704, 2020. [3](#)
- [21] J. Yin, J. Shen, C. Guan, D. Zhou, and R. Yang, "Lidar-based online 3d video object detection with graph-based message passing and spatiotemporal transformer attention," in *IEEE/CVF Conference on Computer Vision and Pattern Recognition*, pp. 11495–11504, 2020. [3](#)
- [22] D. Zhou, J. Fang, X. Song, C. Guan, J. Yin, Y. Dai, and R. Yang, "Iou loss for 2d/3d object detection," in *2019 International Conference on 3D Vision (3DV)*, pp. 85–94, IEEE, 2019. [3](#)
- [23] D. Zhou, J. Fang, X. Song, L. Liu, J. Yin, Y. Dai, H. Li, and R. Yang, "Joint 3d instance segmentation and object detection for autonomous driving," in *the IEEE/CVF Conference on Computer Vision and Pattern Recognition*, pp. 1839–1849, 2020. [3](#)
- [24] C. R. Qi, W. Liu, C. Wu, H. Su, and L. J. Guibas, "Frustum pointnets for 3d object detection from rgb-d data," in *IEEE Conference on Computer Vision and Pattern Recognition*, pp. 918–927, 2018. [3](#)
- [25] B. Graham, M. Engelcke, and L. Van Der Maaten, "3d semantic segmentation with submanifold sparse convolutional networks," in *IEEE conference on computer vision and pattern recognition*, pp. 9224–9232, 2018. [3](#)
- [26] K. Duan, S. Bai, L. Xie, H. Qi, Q. Huang, and Q. Tian, "Centernet: Keypoint triplets for object detection," in *IEEE/CVF International Conference on Computer Vision*, pp. 6569–6578, 2019. [3](#)
- [27] C. R. Qi, H. Su, K. Mo, and L. J. Guibas, "Pointnet: Deep learning on point sets for 3d classification and segmentation," in *IEEE Conference on Computer Vision and Pattern Recognition*, pp. 652–660, 2017. [3](#), [5](#)
- [28] D. Zhou, V. Frémont, B. Quost, and B. Wang, "On modeling ego-motion uncertainty for moving object detection from a mobile platform," in *IEEE Intelligent Vehicles Symposium Proceedings*, pp. 1332–1338, 2014. [3](#)
- [29] M. R. Andreas Geiger and R. Urtasun, "Efficient large-scale stereo matching," in *Proceedings of the Asian Conference on Computer Vision*, pp. 25–38, 2010. [3](#)
- [30] X. Song, W. Li, D. Zhou, Y. Dai, J. Fang, H. Li, and L. Zhang, "Mlda-net: Multi-level dual attention-based network for self-supervised monocular depth estimation," *IEEE Transactions on Image Processing*, vol. 30, pp. 4691–4705, 2021. [3](#)
- [31] F. Chabot, M. Chaouch, J. Rabarisoa, C. Teuliere, and T. Chateau, "Deep manta: A coarse-to-fine many-task network for joint 2d and 3d vehicle analysis from monocular image," in *IEEE conference on computer vision and pattern recognition*, pp. 2040–2049, 2017. [3](#)
- [32] X. Song, P. Wang, D. Zhou, R. Zhu, C. Guan, Y. Dai, H. Su, H. Li, and R. Yang, "Apollocar3d: A large 3d car instance understanding benchmark for autonomous driving," in *IEEE Conference on Computer Vision and Pattern Recognition*, pp. 5452–5462, 2019. [3](#)
- [33] Y. Wang, W.-L. Chao, D. Garg, B. Hariharan, M. Campbell, and K. Q. Weinberger, "Pseudo-lidar from visual depth estimation: Bridging the gap in 3d object detection for autonomous driving," in *IEEE Conference on Computer Vision and Pattern Recognition*, pp. 8445–8453, 2019. [3](#)
- [34] R. Qian, D. Garg, Y. Wang, Y. You, S. Belongie, B. Hariharan, M. Campbell, K. Q. Weinberger, and W.-L. Chao, "End-to-end pseudo-lidar for image-based 3d object detection," in *IEEE/CVF Conference on Computer Vision and Pattern Recognition*, pp. 5881–5890, 2020. [3](#)



- [35] X. Weng and K. Kitani, "Monocular 3d object detection with pseudo-lidar point cloud," in *IEEE/CVF International Conference on Computer Vision Workshops*, pp. 0–0, 2019. [3](#)
- [36] X. Ma, Z. Wang, H. Li, P. Zhang, W. Ouyang, and X. Fan, "Accurate monocular 3d object detection via color-embedded 3d reconstruction for autonomous driving," in *IEEE International Conference on Computer Vision*, pp. 6851–6860, 2019. [3](#)
- [37] Y. Cai, B. Li, Z. Jiao, H. Li, X. Zeng, and X. Wang, "Monocular 3d object detection with decoupled structured polygon estimation and height-guided depth estimation," in *AAAI*, pp. 10478–10485, 2020. [3](#)
- [38] Z. Liu, Z. Wu, and R. Tóth, "Smoke: single-stage monocular 3d object detection via keypoint estimation," in *IEEE/CVF Conference on Computer Vision and Pattern Recognition Workshops*, pp. 996–997, 2020. [3](#)
- [39] D. Zhou, X. Song, Y. Dai, J. Yin, F. Lu, M. Liao, J. Fang, and L. Zhang, "Iafa: Instance-aware feature aggregation for 3d object detection from a single image," in *Asian Conference on Computer Vision*, 2020. [3](#)
- [40] J. Nie, J. Yan, H. Yin, L. Ren, and Q. Meng, "A multimodality fusion deep neural network and safety test strategy for intelligent vehicles," *IEEE Transactions on Intelligent Vehicles*, vol. 6, no. 2, pp. 310–322, 2020. [3](#)
- [41] M. P. Muresan, I. Giosan, and S. Nedevschi, "Stabilization and validation of 3d object position using multimodal sensor fusion and semantic segmentation," *Sensors*, vol. 20, no. 4, p. 1110, 2020. [3](#)
- [42] M. P. Muresan and S. Nedevschi, "Multi-object tracking of 3d cuboids using aggregated features," in *2019 IEEE 15th International Conference on Intelligent Computer Communication and Processing (ICCP)*, pp. 11–18, IEEE, 2019. [3](#)
- [43] X. Du, M. H. Ang, S. Karaman, and D. Rus, "A general pipeline for 3d detection of vehicles," in *2018 IEEE International Conference on Robotics and Automation (ICRA)*, pp. 3194–3200, IEEE, 2018. [3](#)
- [44] X. Chen, H. Ma, J. Wan, B. Li, and T. Xia, "Multi-view 3d object detection network for autonomous driving," in *IEEE Conference on Computer Vision and Pattern Recognition*, pp. 1907–1915, 2017. [3, 7](#)
- [45] K. He, G. Gkioxari, P. Dollár, and R. Girshick, "Mask r-cnn," in *IEEE international conference on computer vision*, pp. 2961–2969, 2017. [3](#)
- [46] M. Liang, B. Yang, Y. Chen, R. Hu, and R. Urtasun, "Multi-task multi-sensor fusion for 3d object detection," in *IEEE Conference on Computer Vision and Pattern Recognition*, pp. 7345–7353, 2019. [3](#)
- [47] R. Nabati and H. Qi, "Centerfusion: Center-based radar and camera fusion for 3d object detection," in *IEEE/CVF Winter Conference on Applications of Computer Vision*, pp. 1527–1536, 2021. [3](#)
- [48] B. Yang, M. Liang, and R. Urtasun, "Hdnet: Exploiting hd maps for 3d object detection," in *Conference on Robot Learning*, pp. 146–155, PMLR, 2018. [4](#)
- [49] J. Fang, D. Zhou, X. Song, and L. Zhang, "Mapfusion: A general framework for 3d object detection with hdm maps," in *IEEE/RSJ International Conference on Intelligent Robots and Systems*, 2021. [4](#)
- [50] A. R. Choudhury, R. Vanguri, S. R. Jambawalikar, and P. Kumar, "Segmentation of brain tumors using deeplabv3+," in *International MICCAI Brainlesion Workshop*, pp. 154–167, Springer, 2018. [4](#)
- [51] H. Zhao, J. Shi, X. Qi, X. Wang, and J. Jia, "Pyramid scene parsing network," in *IEEE conference on computer vision and pattern recognition*, pp. 2881–2890, 2017. [4](#)
- [52] K. Chen, J. Pang, J. Wang, Y. Xiong, X. Li, S. Sun, W. Feng, Z. Liu, J. Shi, W. Ouyang, et al., "Hybrid task cascade for instance segmentation," in *IEEE/CVF Conference on Computer Vision and Pattern Recognition*, pp. 4974–4983, 2019. [4, 8](#)
- [53] E. Shelhamer, J. Long, and T. Darrell, "Fully convolutional networks for semantic segmentation," *IEEE transactions on pattern analysis and machine intelligence*, vol. 39, no. 4, pp. 640–651, 2017. [4](#)
- [54] A. Howard, M. Sandler, G. Chu, L.-C. Chen, B. Chen, M. Tan, W. Wang, Y. Zhu, R. Pang, V. Vasudevan, Q. V. Le, and H. Adam, "Searching for mobilenetv3," in *The IEEE International Conference on Computer Vision (ICCV)*, pp. 1314–1324, October 2019. [4](#)
- [55] Y. Zhang, Z. Zhou, P. David, X. Yue, Z. Xi, B. Gong, and H. Foroosh, "Polarnet: An improved grid representation for online lidar point clouds semantic segmentation," in *IEEE/CVF Conference on Computer Vision and Pattern Recognition*, pp. 9601–9610, 2020. [4](#)
- [56] R. Cheng, R. Razani, E. Taghavi, E. Li, and B. Liu, "2-s3net: Attentive feature fusion with adaptive feature selection for sparse semantic segmentation network," *arXiv preprint arXiv:2102.04530*, 2021. [4](#)
- [57] J. Xu, R. Zhang, J. Dou, Y. Zhu, J. Sun, and S. Pu, "Rpvnet: A deep and efficient range-point-voxel fusion network for lidar point cloud segmentation," *arXiv preprint arXiv:2103.12978*, 2021. [4](#)
- [58] P. Cong, X. Zhu, and Y. Ma, "Input-output balanced framework for long-tailed lidar semantic segmentation," in *2021 IEEE International Conference on Multimedia and Expo (ICME)*, pp. 1–6, IEEE, 2021. [4](#)
- [59] J. Fu, J. Liu, H. Tian, Y. Li, Y. Bao, Z. Fang, and H. Lu, "Dual attention network for scene segmentation," in *Proceedings of the IEEE/CVF Conference on Computer Vision and Pattern Recognition*, pp. 3146–3154, 2019. [6](#)
- [60] A. Geiger, P. Lenz, and R. Urtasun, "Are we ready for autonomous driving? the kitti vision benchmark suite," in *2012 IEEE Conference on Computer Vision and Pattern Recognition*, pp. 3354–3361, IEEE, 2012. [7, 9, 10](#)
- [61] H. Caesar, V. Bankiti, A. H. Lang, S. Vora, V. E. Liong, Q. Xu, A. Krishnan, Y. Pan, G. Baldan, and O. Beijbom, "nuscenes: A multi-modal dataset for autonomous driving," in *Proceedings of the IEEE/CVF conference on computer vision and pattern recognition*, pp. 11621–11631, 2020. [7, 8, 9](#)
- [62] A. Simonelli, S. R. Buló, L. Porzi, M. López-Antequera, and P. Kotschieder, "Disentangling monocular 3d object detection," in *IEEE International Conference on Computer Vision*, pp. 1991–1999, 2019. [7](#)
- [63] L.-C. Chen, Y. Zhu, G. Papandreou, F. Schroff, and H. Adam, "Encoder-decoder with atrous separable convolution for semantic image segmentation," in *ECCV*, 2018. [7](#)
- [64] X. Zhu, H. Zhou, T. Wang, F. Hong, Y. Ma, W. Li, H. Li, and D. Lin, "Cylindrical and asymmetrical 3d convolution networks for lidar segmentation," in *Proceedings of the IEEE/CVF Conference on Computer Vision and Pattern Recognition*, pp. 9939–9948, 2021. [7, 8](#)
- [65] Y. Ma, D. Yu, T. Wu, and H. Wang, "Paddlepaddle: An open-source deep learning platform from industrial practice," *Frontiers of Data and Computing*, vol. 1, no. 1, pp. 105–115, 2019. [8](#)
- [66] Z. Yang, Y. Sun, S. Liu, and J. Jia, "3dssd: Point-based 3d single stage object detector," in *the IEEE/CVF conference on computer vision and pattern recognition*, pp. 11040–11048, 2020. [9](#)
- [67] B. Zhu, Z. Jiang, X. Zhou, Z. Li, and G. Yu, "Class-balanced grouping and sampling for point cloud 3d object detection," *arXiv preprint arXiv:1908.09492*, 2019. [9](#)
- [68] Q. Chen, L. Sun, Z. Wang, K. Jia, and A. Yuille, "Object as hotspots: An anchor-free 3d object detection approach via firing of hotspots," in *European Conference on Computer Vision*, pp. 68–84, Springer, 2020. [9](#)
- [69] Q. Chen, L. Sun, E. Cheung, and A. L. Yuille, "Every view counts: Cross-view consistency in 3d object detection with hybrid-cylindrical-spherical voxelization," *Advances in Neural Information Processing Systems*, vol. 33, 2020. [9](#)
- [70] J. H. Yoo, Y. Kim, J. S. Kim, and J. W. Choi, "3d-cvf: Generating joint camera and lidar features using cross-view spatial feature fusion for 3d object detection," in *Computer Vision - ECCV 2020 - 16th European Conference, Glasgow, UK, August 23–28, 2020, Proceedings, Part XXVII (A. Vedaldi, H. Bischof, T. Brox, and J. Frahm, eds.)*, vol. 12372 of *Lecture Notes in Computer Science*, pp. 720–736, Springer, 2020. [9](#)
- [71] M. Everingham, L. Van Gool, C. K. Williams, J. Winn, and A. Zisserman, "The pascal visual object classes (voc) challenge," *International journal of computer vision*, vol. 88, no. 2, pp. 303–338, 2010. [8](#)
- [72] I. Loshchilov and F. Hutter, "Decoupled weight decay regularization," in *International Conference on Learning Representations*, 2019. [9](#)
- [73] Q.-Y. Zhou, J. Park, and V. Koltun, "Open3d: A modern library for 3d data processing," *arXiv preprint arXiv:1801.09847*, 2018. [11](#)